Targeting Micrometastases: The Effect of Heterogeneous Radionuclide Distribution on Tumor Control Probability

Nadia Falzone[1], Boon Quan Lee[1], Sarah Able[1], Javian Malcolm[1], Samantha Terry[1,2], Yasir Alayed[1], Katherine A. Vallis[1*].

[1]CRUK/MRC Oxford Institute for Radiation Oncology, Oxford University,

Oxford OX3 7DQ, UK

[2]Imaging Chemistry and Biology, King's College London, SE1 7EH, UK

Running title: TCP of micrometastases

Financial Support: This research was supported by CRUK, MRC, and the CRUK Oxford Centre.

[*]Corresponding author:

Katherine A. Vallis,

CRUK/MRC Oxford Institute for Radiation Oncology

Oxford University

Oxford OX3 7DQ

UK

Tel: +44 (0)1865 225850

Email: katherine.vallis@oncology.ox.ac.uk

ABSTRACT

The spatial distribution of radiopharmaceuticals that emit short-range high linear-energy-transfer electrons greatly affects the absorbed dose and their biological effectiveness. The purpose of this study was to investigate the effect of heterogeneous radionuclide distribution on tumor control probability (TCP) in a micrometastases model.

Methods: Cancer cell lines; MDA-MB-468, SQ20B and 231-H2N were grown as spheroids to represent micrometastases. The intracellular distribution of a representative radiopeptide (^{111}In-labelled epidermal growth factor, EGF) and radioimmunotherapeutic (^{111}In-labelled Trastuzumab) was determined in cell internalization experiments. The intratumoral distribution was evaluated by microautoradiography of spheroids. γH2AX staining was performed on spheroid sections to correlate DNA damage with radionuclide distribution. Experimental surviving fractions (SF_{exp}) were obtained using clonogenic assays. A random closed-packed algorithm, which models the random packing behavior of cells and reflects variation in the radii of cells and nuclei, was used to simulate 3-D spheroids. Calculated survival fractions (SF_{cal}) were generated using an iterative modelling method based on Monte Carlo determined absorbed dose with the PENELOPE code and were compared to SF_{exp}. Radiobiological parameters deduced from experimental results and MC simulations were used to predict the TCP for a 3-D spheroid model.

Results: Calculated *SF*s were in good agreement with experimental data, particularly when an increased value for relative biological effectiveness (RBE) was applied to self-dose deposited by sources located in the nucleus and when radiobiological parameters were adjusted to account for dose protraction. Only in MDA-MB-468 spheroids treated with ^{111}In-EGF was a TCP>0.5 achieved, indicating that for this cell type the radiopeptide would be curative when targeting micrometastases. This is attributed to the relative radiosensitivity of MDA-MB-468 cells, high nuclear uptake of the radiopeptide and uniform distribution of radioactivity throughout the spheroid.

Conclusions: It is imperative to include biological endpoints when evaluating the distribution of radionuclides in models emulating micrometastatic disease. The spatial distribution of radioactivity is a clear determinant of biological effect and TCP as demonstrated in this study.

Key words: Auger-electrons, MC modelling, 3-D spheroids, dosimetry, TCP.

INTRODUCTION

The predicted radiobiological effect (RBE) of targeted radionuclide therapy (TRT) is often extrapolated from that of external beam radiotherapy (EBRT). It is assumed that the biological response to TRT will be similar to that of EBRT when an equivalent radiation absorbed dose is delivered to the tumor as a whole. However, the biological response to TRT, varies substantially with differences in expression of the molecular target, which in turn results in spatial non-uniformity of radioactivity and energy deposition and thus absorbed dose (Gy), at the whole tumor, cellular and subcellular levels. It is postulated that Auger electron (AE)-emitting radionuclides that bind or intercalate into DNA are ideal for TRT of single cells, limited volume disseminated cancer and micrometastases (*1*,*2*). This hypothesis is based on the high linear-energy transfer (LET) (4-26 keV/μm) of low-energy AE that deposit energy within a few cubic nanometers of the decay site (*1*,*3*). The localized absorption of electrons results in complex irreparable DNA damage (*4*). This feature endows AE-emitting TRT agents with an enhanced RBE when compared to α- or β-emitting radionuclides.

To advance our understanding of the radiobiology of AE-emitting therapeutics and to test the hypothesis that they are ideally suited to the treatment of micrometastases, appropriate biological models that reflect the *in vivo* 3-D architecture and physiology of tumors are required. Also, a dosimetric approach, which takes account of both the intratumoral *and* intracellular distribution of radioactivity, is necessary (*5*). Multicellular tumor spheroids are excellent models of micrometastases as they reflect the cellular heterogeneity, physiological gradients (*6*,*7*) and resistance to therapy of small tumors (*8*). By combining experimental data detailing the dose distribution in individual cells and in whole spheroids with Monte Carlo (MC) modelling, radiobiological quantities such as tumor control probability (TCP), that relate the fate of individual cells to a macroscopic outcome, can be calculated (*9*,*10*). Several MC studies focusing on the charge transport of AE in volumes representing small cell clusters have explored whether the dose deposited would be sufficient to illicit a tumoricidal effect (*11*,*12*). However, to date only a few studies have attempted to validate MC simulations that predict the efficacy of AE-emitters with experimental observations (*13*-*15*).

In this study the efficacy of radiolabeled peptide- and antibody-based constructs was evaluated in spheroids generated from three cancer cell lines. ^{111}In-DTPA-human epidermal growth factor (hereafter "^{111}In-EGF"), which causes selective radiotoxicity in EGF receptor

(EGFR)-overexpressing cells, was used as a representative radiopeptide and ^{111}In-DTPA-Trastuzumab (hereafter "^{111}In-Tz"), which binds the human EGFR-2 (HER2/neu) receptor, was used as a representative radioimmunotherapeutic (*16,17*). Data derived from cell internalization and spheroid microautoradiography (MAR) experiments were used to build realistic *in silico* MC models. These models were used to predict TCP and validated against experimentally derived values.

MATERIALS AND METHODS

3-D Culture of Spheroids

Human breast cancer cell lines MDA-MB-468 ($1.3x10^6$ EGFR/cell; HER2 low) and 231-H2N ($0.2x10^6$ EGFR, $6.1x10^5$ HER2/cell) and a human head and neck squamous carcinoma cell line, SQ20B ($1.0x10^6$ EGFR/cell, HER2 low) (*16,18*), were grown in Dulbecco's Modified Eagle's Medium (Sigma-Aldrich, Dorset, UK) supplemented with 10% fetal bovine serum (FBS; Invitrogen, Paisley, UK), 100 units/mL penicillin and 100 µg/mL streptomycin (Sigma-Aldrich) at 37°C in 5% CO_2. MDA-MB-468 and SQ20B cells were obtained from American Type Culture Collection, 231-H2N cells from Robert Kerbel, Sunnybrook Health Sciences Centre, Toronto. Spheroids were generated using the InSphero hanging droplet method. MDA-MB-468 (10,000 cells/well), 231-H2N (40,000 cells/well in InSphero 3-D culture medium) and SQ20B (20,000 cells/well) were seeded into GravityPLUS™ plates (InSphero AG, Zurich, Switzerland). Spheroids were transferred to GravityTRAP™ plates on Day 4.

Microautoradiography and Immunofluorescence

Synthesis of ^{111}In-EGF and ^{111}In-Tz was performed as previously described (*16,19*). Spheroids were exposed to ^{111}In-EGF (8 MBq/µg; 40 nM) or ^{111}In-Tz (6 MBq/µg; 10 nM) for 1 or 24 h and then fixed for 30 min (4% paraformaldehyde), washed in PBS and placed in a cryomould (Agar scientific, UK) containing Tissue Tek O.C.T. (Electron Microscopy Sciences, PA, USA). Samples were flash frozen and stored at -80ºC. Samples were sectioned into 8 µm-thick sections, thaw mounted on Superfrost® Plus microscopy slides (VWR Int., Leuven, Belgium) and dried at room temperature for at least 30 min before coating with Kodak NTB emulsion (VWR Int., Leicestershire, UK). Slides were stored in a light tight box for 24 h at 2-8°C until development (Kodak D-19, Sigma-Aldrich) and fixation (Kodak

polymer RT, 1:4, Sigma-Aldrich). γH2AX staining was performed as previously described (*18*) on sequential spheroid sections to evaluate DNA damage.

Sub-Cellular Distribution of Radioactivity

Cells ($1x10^6$ cells/mL), were exposed to ^{111}In-EGF (8 MBq/μg; 40 nM) or ^{111}In-Tz (6 MBq/μg; 10 nM) for 1 or 24 h. Unbound, membrane-bound, cytoplasmic and nuclear fractions were collected as previously described (*16*) and using a Subcellular Protein Fractionation Kit (Thermo Fischer). Purity of fractions was confirmed by western blot analysis of known membrane, cytoplasmic and nuclear proteins: beta integrin, alpha tubulin and H2AX. The amount of radioactivity in each fraction was measured by γ-counter (PerkinElmer Wizard 1470, Waltham, MA, USA).

Cell Size Measurement

Cells were cytospun onto slides and fixed (4% PFA, Sigma-Aldrich) for 15 min at 37˚C. After washing with PBS, cells were covered in a membrane specific stain, wheat germ agglutinin (5.0 μg/mL) conjugate (WGA-Alexa Flour-488, Thermo Fisher Scientific, Basingstoke, UK) for 10 min followed by DAPI staining of cell nuclei. Cells were washed in PBS and mounted with Vectashield mounting medium (Vector Laboratories, Peterborough, UK) before microscopy (TCS SP2 microscope, Leica Microsystems, UK). Cell and nuclei radii were taken as the average of n=30 stained cells.

MC Simulation

To represent 3-D spheroids *in silico*, an event-driven molecular dynamics algorithm (*20*) for a system of monodisperse spherical random close-packed (RCP) cells was used (*21*,*22*). Event-by-event simulation was performed using the MC code PENELOPE (*23*) and the complete electron spectrum of ^{111}In based on the unabridged nuclear decay data (*BrIccEmis*) (*24*). The photon absorbed fraction was negligible and therefore omitted (*5*). A total of $1x10^8$ primary particles were simulated. Simulations were performed in liquid water and the spatial distribution of radioactivity within a spheroid was based on MAR results. Two scenarios were considered (reflecting MAR staining): uniform distribution of radioactivity throughout the spheroid or peripheral accumulation. The radioactivity in each cell of the MC model was informed by experimental sub-cellular internalization data. Absorbed fractions (*S*-values), derived from dose-point kernels of an ^{111}In point source in liquid water using the terminology described in (*1*), were calculated for contributions from a source cell to its nucleus (N←Cs),

the cytoplasm to its nucleus (N←Cy) and the nucleus to itself (N←N). The cross-dose was derived from the difference between the self-dose and simulated total dose (*25*). *S*-values were calculated for single cells, monolayers and cell clusters, the latter two using the RCP algorithm.

Survival Fraction and Tumor Control Probability Calculation

Clonogenic survival assays were performed on monolayers of MDA-MB-468, SQ20B and 231-H2N cells treated with ^{111}In-EGF (8 MBq) or ^{111}In-Tz (6 MBq) as previously described (*16*). The radiosensitivity parameters, α and β, were determined for each cell line after ^{137}Cs irradiation (1 Gy/min) by fitting the average SF from three independent experiments using least-squares regression by the linear quadratic model. α and β values were 0.46 and 0.003 for MDA-MB-468, 0.20 and 0.001 for SQ20B and 0.12 and 0.06 for 231-H2N cells.

The survival probability of an individual cell, SP_i, follows the linear-quadratic model (LQM) (*9*);

$$SP_i = e^{-(\alpha D_i + \beta G D_i^2)} \quad (1)$$

with D_i the absorbed dose (Gy) of an individual cell, α and β determined from ^{137}Cs irradiation and G the Lea-Catcheside factor which accounts for radiation damage repair (Supplemental Material). Dose was calculated according to the MIRD formulation (*26*), where D_i is taken as the product of accumulated activity $\tilde{A}$ in each cell compartment with its associated *S*-value, where τ is the target (nucleus) and σ the source (i.e. N, Cy or Cs);

$$D_i = \sum_i \tilde{A}_{\sigma_i} \times S(\tau \leftarrow \sigma_i) \quad (2)$$

For a population of N_c identical clonogenic cells that receive a variable absorbed dose, D_i, the calculated surviving fraction (*SF*), SF_{cal} of the population is

$$SF_{cal} = \frac{\sum_{i=1}^{N_c} SP_i}{N_c} \quad (3)$$

Thus the TCP of a 3-D spheroid, which is defined as the probability of killing all cells within the spheroid, is given as

$$\mathrm{TCP} = \prod_{i=1}^{N_c}(1 - SP_i) \quad (4)$$

Statistical Analysis

Statistical analyses were performed using GraphPad Prism® (version 5, GraphPad Software, Inc, USA). Internalization and clonogenic SF data were analysed using two-way ANOVA with Sidak's multiple comparisons test and Tukey's multiple comparison test respectively. Statistical significance is reported as $p<0.05$.

RESULTS

3-D Spheroid Model

A 3-D rendering of an *in silico* MDA-MB-468 spheroid, a cross section through a smaller cluster (to demonstrate variation in cell and nucleus size), and the relationship between radii of cells and nuclei are shown in Fig. 1. MDA-MB-468 spheroids comprised of loosely associated cells compared to 231-H2N and SQ20B spheroids (Fig. 2A-C). SQ20B cells formed spheroids with a rim of tightly packed cells with less densely packed cells toward the center. Cell and nucleus radii (R_c, R_n) in µm used for MC simulations were; MDA-MB-468: R_c=9.45±1.71, R_n=6.65±1.30; SQ20B: R_c=10.61±1.24, R_n=8.10±1.39 and 231-H2N: R_c=11.21±2.59, R_n=7.09±1.44 (Fig. 2D-F). The radius of each cell and corresponding nucleus were sampled from an empirical distribution of the cell line radii, taking into consideration the correlation between the two (Supplemental Fig. 1).

Radioactivity Uptake and DNA Damage in Spheroids

^{111}In-EGF: At 1 h, ^{111}In-EGF accumulated at the periphery of EGFR-positive MDA-MB-468 and SQ20B spheroids (Figs. 3A and 4A). Control untreated spheroids are shown for comparison (inset images, Figs. 3A and 4A). By 24 h, ^{111}In-EGF had accumulated throughout MDA-MB-468 spheroids (Fig. 3B), while peripheral accumulation persisted in SQ20B spheroids (Fig. 4B). γH2AX induction reflected radioactivity distribution, and at 24 h was observed throughout MDA-MB-468 spheroids (Fig. 3C), but was restricted to the periphery in SQ20B spheroids (Fig. 4C). The amount of ^{111}In-EGF that had accumulated in whole cells and in membrane, cytoplasmic and nuclear fractions by 1 and 24 h is shown for MDA-MB-468 (Figs. 3D) and SQ20B cells (Fig. 4 D). In MDA-MB-468 cells, membrane and cytoplasmic fractions increased significantly with time ($p<0.0001$). Nuclear accumulation remained virtually constant in SQ20B cells, while the cytoplasmic fraction increased significantly with time ($p<0.0001$). EGFR-low 231-H2N cells showed minimal ^{111}In-EGF internalization, while spheroids showed little MAR (Supplemental Fig. 2) or γH2AX staining (data not shown).

^{111}In-Tz: There was little MAR staining and accumulation of ^{111}In-Tz in the HER2-low cell lines MDA-MB-468 or SQ20B (Supplemental Fig. 3). Peripheral accumulation of radioactivity was seen after 1 h incubation in HER2-high 231-H2N spheroids (Fig. 5A), with even distribution throughout the spheroid by 24 h (Fig. 5B). It is possible that the relatively sparse γH2AX staining in HER2-high 231-H2N (Fig. 5C) compared to MDA-MB-468 spheroids, despite uniform and marked accumulation of radioactivity throughout the whole spheroid, could be explained by the relatively low nuclear accumulation of ^{111}In in 231-H2N versus MDA-MB-468 cells.

Clonogenic Survival

Following exposure to ^{111}In-EGF the surviving fraction (SF) of MDA-MB-468 cells decreased to 71±10% after 1 h ($p<0.001$), and to 1±1% ($p<0.0001$) after 24 h (Fig. 6A). For SQ20B cells, *SF* was 9±3 % at 24 h ($p<0.0001$). 231-H2N cells express the smallest number of EGFR and internalized the least activity; this is reflected in the SF of 99±5 % at 24 h.

^{111}In-Tz did not have a statistically significant effect on SF in the HER2-low cell lines MDA-MB-468 and SQ20B (Fig. 6B). However, cell survival in the HER2-positive cell line, 231-H2N, was significantly different at 24 h compared to 1 h ($p<0.0001$), with SF decreasing to 46±9 % at 24 h.

MC simulation

S-values: MC calculated *S*-values for single cells, monolayers and cell clusters are summarized in Table 1. Single-cell *S*-values are in good agreement with MIRDCell values with differences ≤ 2%. RCP *S*-values for monolayers and clusters take cross-fire from neighboring cells into account. As a result of the variation in cell size and RCP, *S*-values are given as an average value and standard deviation. The greatest effect of crossfire was noted in cytoplasmic and cell-surface contributions, where *S*(N←Cy) increased by at least a factor of two in monolayer and almost a factor of 3 in spheroids across all cell lines, when compared with single cell *S*-values. In the case of 231-H2N, *S*(N←Cs) contribution from RCP increased almost 5-fold compared to single cells. A graphical illustration of the contribution of cross dose to the total dose for cell clusters as a function of a radial distance from spheroid center, is shown in Supplemental Fig. 4 and the total contributions are summarized in Supplemental Table 1.

SF and TCP evaluation: Cell compartment-specific uptake of the peptide and antibody constructs was evaluated to inform MC calculated *SF* (SF_{cal}). Trapezoidal integration of the total activity at 1 and 24 h in the different cellular compartments provided the data necessary to calculate accumulated activity ($\tilde{A}$) (Table 2). Absorbed dose was then calculated (equation 2) and SF_{cal} determined using *S*-values for 3-D spheroids (Table 2). Assumptions made were that the activity internalized in a single cell is representative of that in cells within a spheroid and that the experimental *SF* (SF_{exp}) determined for monolayers is applicable to spheroids.

SF_{exp} (Fig. 6) and SF_{cal} were compared with MIRDcell calculated *SF* (Table 2) (*12*). MC model 1, $MC_{(1)}$, and MIRDcell are both based on α- and β-values derived from ^{137}Cs irradiation, the only difference being the packing algorithms used. MIRDcell assumes uniform cell and nucleus sizes in a close-packed cubic lattice. Across all cell lines the 1 h SF data of MIRDcell and $MC_{(1)}$ are in good agreement (<5% difference). However, MIRDcell SF are consistently lower (by up to 40%) at 24 h compared to $MC_{(1)}$. This is partly due to the higher cross-dose contribution from cubic lattice packing compared to RCP and the variation in cell/nucleus size in the RCP cluster. If a threshold dose is required to kill a cell of a certain size, smaller cells will be killed but not bigger cells – with uniform cell sizes, all cells reaching that threshold dose will die. Neither model however, predicts SF_{exp} adequately. The second iteration, $MC_{(2)}$ assumes a greater RBE when AE-emitters accumulate in the nucleus of a cell. $MC_{(2)}$ and SF_{exp} are in good agreement across all cell lines apart from 24 h SF data for the radioresistant cell line 231-H2N. This discrepancy can be attributed to the combination of the suppressed Lea-Catcheside factor, G (Supplemental Material Eq. 1) following 24 h of low-dose-rate exposure and radioresistance of the 231-H2N cell line (low α/β ratio and high β). The next iteration, $MC_{(3)}$ is similar to $MC_{(2)}$ but also accounts for the suppression of G factor following exposure to ^{111}In for 1 and 24 h. $MC_{(3)}$ only differs significantly from $MC_{(2)}$ for 231-H2N cells and the *SFs* derived using this model are in good agreement with the SF_{exp}.

When radioactivity is restricted to the periphery of the spheroids, the calculated TCP becomes zero. If physical decay alone is considered, and no further internalization of ^{111}In-conjugated constructs is allowed after 24 h, only MDA-MB-468 spheroids exposed to ^{111}In-EGF, achieve a TCP of 50% for all three MC models (after 5.3, 1.9 and 2 days for $MC_{(1)}$, $MC_{(2)}$ and $MC_{(3)}$, respectively). This is evident from Fig. 7 where unlabeled cells receive negligible doses due to the weak cross-fire effect associated with ^{111}In.

DISCUSSION

Here, the efficacy of a peptide and antibody delivery strategy for AE-targeted radiotherapy was evaluated in spheroid models of three different cell lines, namely; MDA-MB-468, SQ20B and 231-H2N. Spheroid morphology was then used to generate 3-D geometry models for MC simulation to predict TCP using data from activity distribution, internalization and survival assays to build realistic *in silico* models.

It was immediately evident that spheroid morphology differed between cell lines. MDA-MB-468 cells did not form compact round spheroids as was the case with the other breast cancer cell line, 231-H2N, (Fig. 2) but rather loosely aggregated cells, a characteristic previously observed by Ivascu et al (*6*). This loose aggregation of cells facilitated the penetration of the ^{111}In-labelled peptide as seen on MAR images, which showed a large accumulation of silver grains on the rim of MDA-MB-468 spheroids after a 1 h incubation with ^{111}In-EGF which spread over the whole spheroid section after incubation for 24 h (Fig. 3A and B). In contrast, SQ20B speheroids consisted of tightly packed cells at the periphery compared with the core. It is possible that the dense outermost cell layers established a diffusion barrier, which prohibited the penetration of the radiopeptide. MAR results confirmed that the accumulation of silver grains were mostly restricted to the rim of the spheroid at 1 and 24 h (Fig. 4A and B). The EGFR-low cell line, 231-H2N, showed little positive MAR staining at either time point (Supplemental Fig. 3). The situation was reversed when evaluating the spatial distribution of the ^{111}In-labelled antibody, ^{111}In-Tz. HER2-low cell lines, MDA-MB-468 and SQ20B showed barely any MAR staining at 1 and 24 h (Supplemental Fig. 4) whereas ^{111}In-Tz treated 231-H2N spheroids showed a peripheral staining pattern at 1 h which spread throughout the spheroid at 24 h (Fig. 5 A and B).

MAR staining, although informative, does not take into account the non-uniform radionuclide distribution within individual cells which could significantly alter the energy deposition in the cell (or cell nucleus), especially in the context of short-range electron emission (*13*). Hence, MAR staining was used to provide a global representation of activity distribution, while internalization assays provided activity distribution at a sub-cellular level. To confirm that activity distribution correlated with DNA damage, γH2AX staining was performed. γH2AX staining patterns for ^{111}In-EGF-treated MDA-MB-468 and SQ20B spheroids after 24 h correlated well with MAR, showing γH2AX induction throughout the MDA-MB-468 spheroid and peripheral induction only in the SQ20B spheroid. There was less γH2AX

induction in SQ20B cells compared with MDA-MB-468 cells as the latter accumulated almost twice the nuclear activity. With ^{111}In-Tz-treated 231-H2N spheroids, γH2AX foci (Fig. 5C) were sparsely distributed compared to ^{111}In-EGF-treated MDA-MB-468 spheroids (Fig. 3C), which was initially surprising given the uniform MAR staining in both spheroid models. On closer inspection it is clear from internalization data that most of the activity was bound to the surface of 231-H2N cells, which would explain the less abundant γ-H2AX staining.

To relate accumulated activity with cell survival after 1 and 24 h treatment with the ^{111}In-labelled peptide and antibody constructs, clonogenic assays were performed using cells grown in monolayers (Fig. 6). An assumption made here is that *SFs* measured in monolayers can be extrapolated to 3-D spheroids given the same subcellular distribution of activity. It would of course be more informative to use treated spheroids for clonogenic assays, however in our hands disaggregation of spheroids after radionuclide treatment lead to significant cell loss with the result that colony counting experiments were not reproducible. Rae and Mairs (*27*) recently discussed the utility of using a multicellular spheroid growth assay as an alternative measure of clonogenicity. However, since our endpoint was to determine TCP of the different AE-treatment strategies, estimation of clonogenic *SF* was necessary. These data were then used with MC calculated *S*-values to estimate absorbed dose. In addition, these data were compared with MIRDCell data. The MIRDcell software provides estimates of *S*-values in single cells, cell-monolayers and cells cluster in a close-packed geometry, and predicts the *SF* of targeted and non-targeted cell populations in the latter (*12*). Although close-packed hexagonal or cubic lattices as used by MIRDcell are mathematically simpler models than RCP algorithms, they do not reflect the disorganized cellular architecture of tumors, nor do they account for the non-uniform distribution of cell/nucleus sizes (*28,29*). *S*-values are greatly affected by cell volume, thus *S*-values (and hence dose) may be significantly under- or over-estimated when variation in cell volume is ignored. Furthermore, activity is often assumed to be homogeneously distributed to simplify simulation. Here we have determined the intracellular distribution of activity in individual cells as well as the spatial distribution by MAR in tumor spheroids. By incorporating the experimentally determined radioactivity distribution with robust MC simulation, it is possible to construct models to predict radiobiological endpoints. For this reason monodisperse spherical RCP cells reflecting the variation in cell/nuclei radii and radioactivity distribution were used to generate monolayer and 3-D MC spheroid models.

When comparing $MC_{(1)}$ calculated SF_{cal} after 1 h incubation with ^{111}In-EGF to experimental results (Table 2), we note differences of up to 33% for MDA-MB-468. In contrast, Cai *et al* (*14*) reported differences of less than 4% between MC calculated and experimental results. The main contributing factors for these discrepancies can be ascribed to the bigger cell radii reported in this paper and activity estimation, which was determined by trapezoidal integration in this instance and not assuming instantaneous uptake. When taking these two factors into consideration, SF_{cal} does not adequately predict SF_{exp}.

One aspect that we have not addressed is the adoption of radiosensitivity parameters for the different cell lines generated by ^{137}Cs irradiation. With a protracted radiation delivery as is the case with TRT, radiation repair will occur and the Lea-Catcheside factor can no longer be assumed to be 1 (Supplemental Table 2). Furthermore, the α-component from high dose rate ^{137}Cs-irradiation is likely to overestimate the radiosensitivity compared to internalized ^{111}In apart from the scenario where ^{111}In is incorporated or close to the DNA in the nucleus. It has been noted that there is a difference in radiotoxicity arising from self- and cross-irradiation, especially with AE-emitting radionuclides associated with the DNA (*30*). To account for this, $MC_{(2)}$ incorporated RBE-adjusted α/β ratios for nucleus associated AE-emitters, with subsequent good correlation with experimental *SF*s. A further iteration, $MC_{(3)}$, which took repair into consideration, resulted in an even better prediction of SF_{exp}. However, TCP probability estimates (Fig. 7) clearly show that only those cells with a high enough nuclear activity uptake will accumulate a lethal dose, while neighboring cells are spared (*15*,*31*).

Considering that spheroids are representative of micrometastases in their pre-vascular stage of development, the results observed here confirm that the single most important aspect that will determine the biological efficacy of an AE-emitting targeting strategy is the uniform nuclear accumulation of the construct. Even though ^{111}In-Tz was uniformly distributed throughout the 231-H2N spheroid, TCP was not achieved as a result of limited nuclear accumulation. Similarly, while EGFR expression level is similar in SQ20B and MDA-MB-468 cells, the nuclear accumulation of ^{111}In-EGF was much less for SQ20B than MDA-MB-468. Also the 3-D morphology of the spheroid prohibited adequate penetration of ^{111}In-EGF resulting in a negligible TCP. Given these results, it is plausible that an AE-emitting TRT agent could be used in a clinical scenario to target limited volume disseminated cancer and micrometastases. Indeed, in the first-in-human trial using ^{111}In-EGF tumor localization was achieved without any serious adverse effects (*32*).

CONCLUSION

It is essential when evaluating the distribution of radionuclides in models of micrometastatic disease to include biological endpoints such as TCP. As shown here, the spatial distribution of radioactivity at sub-cellular and multi-cellular levels are a clear indicator of biological effect and TCP.

DISCLOSURE

The authors have nothing to disclose.

ACKNOWLEDGEMENTS

This work was supported by grants from Cancer Research UK (CRUK) (C5255/A15935), the Medical Research Council (MRC) (MC-PC-12004) and the CRUK Oxford Centre.

REFERENCES

1. Gill MR, Falzone N, Du Y, Vallis KA. Targeted radionuclide therapy in combined-modality regimens. *Lancet Oncol.* 2017;18:e414-e423.

2. Zanzonico P. Cell level dosimetry and biologic response modeling of heterogeneously distributed radionuclides: A step forward. *J Nuc Med.* 2011;52:845-847.

3. Falzone N, Fernandez-Varea JM, Flux G, Vallis KA. Monte Carlo evaluation of Auger electron-emitting theranostic radionuclides. *J Nucl Med.* 2015;56:1441-1446.

4. Buchegger F, Perillo-Adamer F, Dupertuis YM, Delaloye AB. Auger radiation targeted into DNA: a therapy perspective. *Eur J Nucl Med Mol Imaging.* 2006;33:1352-1363.

5. Rajon D, Bolch WE, Howell RW. Lognormal distribution of cellular uptake of radioactivity: Monte Carlo simulation of irradiation and cell killing in 3-dimensional populations in carbon scaffolds. *J Nucl Med.* 2011;52:926-933.

6. Ivascu A, Kubbies M. Rapid generation of single-tumor spheroids for high-throughput cell function and toxicity analysis. *J Biomol Screen.* 2006;11:922-932.

7. Ivascu A, Kubbies M. Diversity of cell-mediated adhesions in breast cancer spheroids. *Int J Oncol.* 2007;31:1403-1413.

8. Nath S, Devi GR. Three-dimensional culture systems in cancer research: Focus on tumor spheroid model. *Pharmacol Ther*. 2016;163:94-108.

9. Hobbs RF, Baechler S, Fu DX, et al. A model of cellular dosimetry for macroscopic tumors in radiopharmaceutical therapy. *Med Phys.* 2011;38:2892-2903.

10. Ingargiola M, Runge R, Heldt JM, et al. Potential of a Cetuximab-based radioimmunotherapy combined with external irradiation manifests in a 3-D cell assay. *Int J Cancer*. 2014;135:968-980.

11. Bousis C, Emfietzoglou D, Nikjoo H. Calculations of absorbed fractions in small water spheres for low-energy monoenergetic electrons and the Auger-emitting radionuclides ^{123}I and ^{125}I. *Int J Rad Biol.* 2012;88:916-921.

12. Vaziri B, Wu H, Dhawan AP, Du P, Howell RW. MIRD Pamphlet No. 25: MIRDcell V2.0 software tool for dosimetric analysis of biologic response of multicellular populations. *J Nucl Med.* 2014;55:1557-1564.

13. Arnaud FX, Paillas S, Pouget JP, Incerti S, Bardiès M, Bordage MC. Complex cell geometry and sources distribution model for Monte Carlo single cell dosimetry with iodine 125 radioimmunotherapy. *Nucl Instrum Methods Phys Res B.* 2016;366:227-233.

14. Cai Z, Pignol JP, Chan C, Reilly RM. Cellular dosimetry of (111)In using monte carlo N-particle computer code: comparison with analytic methods and correlation with in vitro cytotoxicity. *J Nucl Med.* 2010;51:462-470.

15. Reijonen V, Kanninen LK, Hippeläinen E, et al. Multicellular dosimetric chain for molecular radiotherapy exemplified with dose simulations on 3D cell spheroids. *Physica Medica*. 2017;40:72-78.

16. Cornelissen B, Darbar S, Hernandez R, et al. ErbB-2 blockade and prenyltransferase inhibition alter epidermal growth factor and epidermal growth factor receptor trafficking and enhance (111)In-DTPA-hEGF Auger electron radiation therapy. *J Nucl Med.* 2011;52:776-783.

17. Reilly R, Kiarash R, Cameron R, et al. ^{111}In-labeled EGF is selectively radiotoxic to human breast cancer cells overexpressing EGFR. *J Nucl Med.* 2000;41:429-438.

18. Cornelissen B, Waller A, Able S, Vallis KA. Molecular radiotherapy using cleavable radioimmunoconjugates that target EGFR and gammaH2AX. *Mol Cancer Ther*. 2013;12:2472-2482.

19. Costantini DL, Bateman K, McLarty K, Vallis KA, Reilly RM. Trastuzumab-resistant breast cancer cells remain sensitive to the auger electron-emitting radiotherapeutic agent 111In-NLS-trastuzumab and are radiosensitized by methotrexate. *J Nucl Med.* 2008;49:1498-1505.

20. Lubachevsky B, Stillinger F, Pinson E. Disks vs. spheres: Contrasting properties of random packings. *J Stat Phys.* 1991;64:501-524.

21. Donev A, Stillinger FH, Torquato S. Pair correlation function characteristics of nearly jammed disordered and ordered hard-sphere packings. *Phys Rev E.* 2005;71:011105.

22. Donev A, Stillinger FH, Torquato S. Neighbor list collision-driven molecular dynamics simulation for nonspherical particles. I. Algorithmic details II. Applications to ellipses and ellipsoids. *J Comp Phys.* 2005:202:737-764 (part I) and 202(732):765-793 (part II).

23. Salvat F, Fernandez-Varea JM, Sempau J. PENELOPE-2011: A code system for Monte Carlo simulation of electron and photon transport. 2011, OECD Nuclear Energy Agency, Issy-les-Moulineaux.

24. Lee B, Nikjoo H, Ekman J, Jönsson P, Stuchbery A, Kibédi T. A stochastic cascade model for Auger-electron emitting radionuclides. *Int J Rad Biol.* 2016;92 641-653.

25. Goddu SM, Rao DV, Howell RW. Multicellular dosimetry for micrometastases: dependence of self-dose versus cross-dose to cell nuclei on type and energy of radiation and subcellular distribution of radionuclides. *J Nucl Med.* 1994;35:521-530.

26. Goddu SM, Howell RW, Bouchet LG, Bolch WE, Rao DV. MIRD cellular S values. Reston, VA: Society of Nuclear Medicine; 1997.

27. Rae C, Mairs RJ. Evaluation of the radiosensitizing potency of chemotherapeutic agents in prostate cancer cells. *Int J Radiat Biol.* 2017;93:194-203.

28. Marcatili S, Pichard A, Courteau A, et al. Realistic multi-cellular dosimetry for 177 Lu-labelled antibodies: model and application. *Phys Med Biol.* 2016;61:6935.

29. Poole CM, Ahnesjo A, Enger SA. Determination of subcellular compartment sizes for estimating dose variations in radiotherapy. *Radiat Prot Dosimetry.* 2015;166:361-364.

30. Howell RW, Neti PVSV. Modeling multicellular response to nonuniform distributions of radioactivity: Differences in cellular response to self-dose and cross-dose. . *Radiat Res*. 2005;163:216-221.

31. Walrand S, Hanin F-X, Pauwels S, Jamar F. Tumour control probability derived from dose distribution in homogeneous and heterogeneous models: assuming similar pharmacokinetics, (125)Sn–(177)Lu is superior to (90)Y–(177)Lu in peptide receptor radiotherapy. *Phys Med Biol.* 2012;57:4263.

32. Vallis KA, Reilly RM, Scollard D, et al. Phase I trial to evaluate the tumor and normal tissue uptake, radiation dosimetry and safety of (111)In-DTPA-human epidermal growth factor in patients with metastatic EGFR-positive breast cancer. *Am J Nucl Med Mol Imaging.* 2014;4:181-192.

33. Howell RW, Rao DV, Hou DY, Narra VR, Sastry KS. The question of relative biological effectiveness and quality factor for Auger emitters incorporated into proliferating mammalian cells. *Radiat Res.* 1991;128:282-292.

34. Kriehuber R, Riedling M, Simko M, Weiss DG. Cytotoxicity, genotoxicity and intracellular distribution of the Auger electron emitter (65)Zn in two human cell lines. *Radiat Environ Biophys.* 2004;43:15-22.

FIGURE LEGENDS

FIGURE 1. (A) Packing of monodisperse spherical RCP cells according to the cell size distribution of the MDA-MB-468 cell line. (B) Cross-section through a spheroid showing the variation of cell and nucleus radii according to their Gaussian distribution. (C) Distribution of sampled cell and nucleus radii of the MDA-MB-468 cell line.

FIGURE 2. Light microscopy images showing 3-D spheroids of (A) MDA-MB-468, (B) SQ20B and (C) 231-H2N produced using the hanging droplet method (scale bar: 100 µm). Confocal microscopy images of associated cell sizes, membrane (green - wheat germ agglutinin) and nuclei (blue - DAPI) for (D) MDA-MB-468, (E) SQ20B and (F) 231-H2N (scale bar: 20 µm).

FIGURE 3. Spatial distribution of ^{111}In-EGF in MDA-MB-468 spheroids. Microautoradiograms of 8 µm spheroid sections after (A) 1 h (insert shows control) and (B) 24 h treatment. (C) γH2AX expression in consecutive spheroid section after 24 h treatment – insert shows uniform distribution of foci within cells throughout the spheroid. (D) Internalized activity (mBq/cell) determined at 1 and 24 h incubation. *$p<0.05$, ns = not significant.

FIGURE 4. Spatial distribution of ^{111}In-EGF in SQ20B spheroids. Microautoradiograms of 8 µm spheroid sections after (A) 1 h (insert shows control) and (B) 24 h treatment. (C) γH2AX expression in consecutive spheroid section after 24h treatment – insert shows peripheral distribution of foci within the spheroid. (D) Internalized activity (mBq/cell) determined at 1 and 24 h incubation. *$p<0.05$, ns = not significant.

FIGURE 5. Spatial distribution of ^{111}In-Tz in 231-H2N spheroids. Microautoradiograms of 8 µm spheroid sections after (A) 1 h (insert shows control) and (B) 24 h treatment. (C) γH2AX expression in consecutive spheroid section after 24 h treatment. (D) Internalized activity (mBq/cell) determined at 1 and 24 h incubation. *$p<0.05$, ns = not significant.

FIGURE 6. Clonogenic survival of MDA-MB-468, SQ20B and 231-H2N cells after 1 or 24 h treatment with (A) ^{111}In-EGF (8 MBq/µg, 40 nM) or (B) ^{111}In-Tz (6 MBq/µg, 10 nM). Error bars: SD of mean *SF*, n = 3.

FIGURE 7. MC-simulated dose histograms of (A) MDA-MB-468 and (B) SQ20B spheroids after 24 h exposure to ^{111}In-EGF and TCP for each dose bin of 0.5 Gy (right vertical axis).

FIGURES

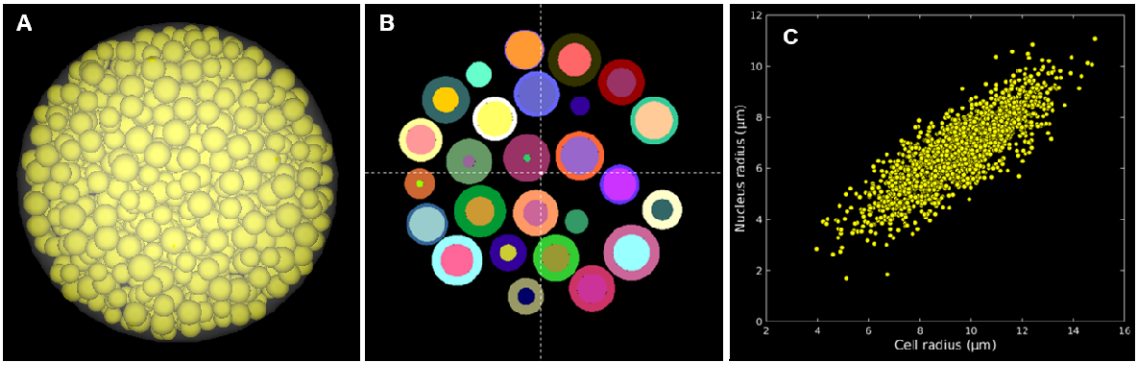

FIGURE 1.

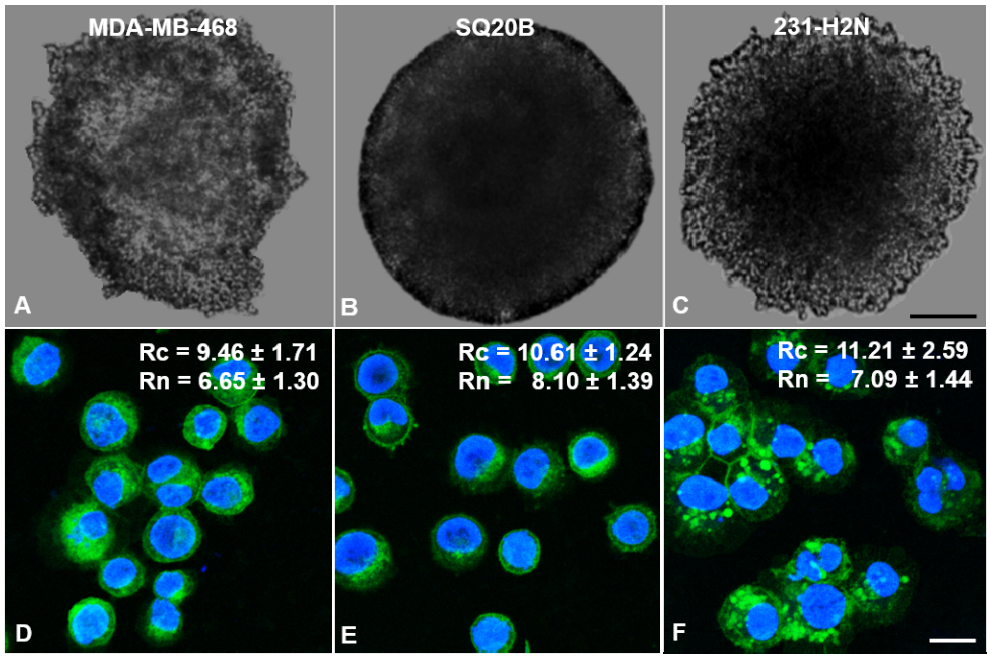

FIGURE 2.

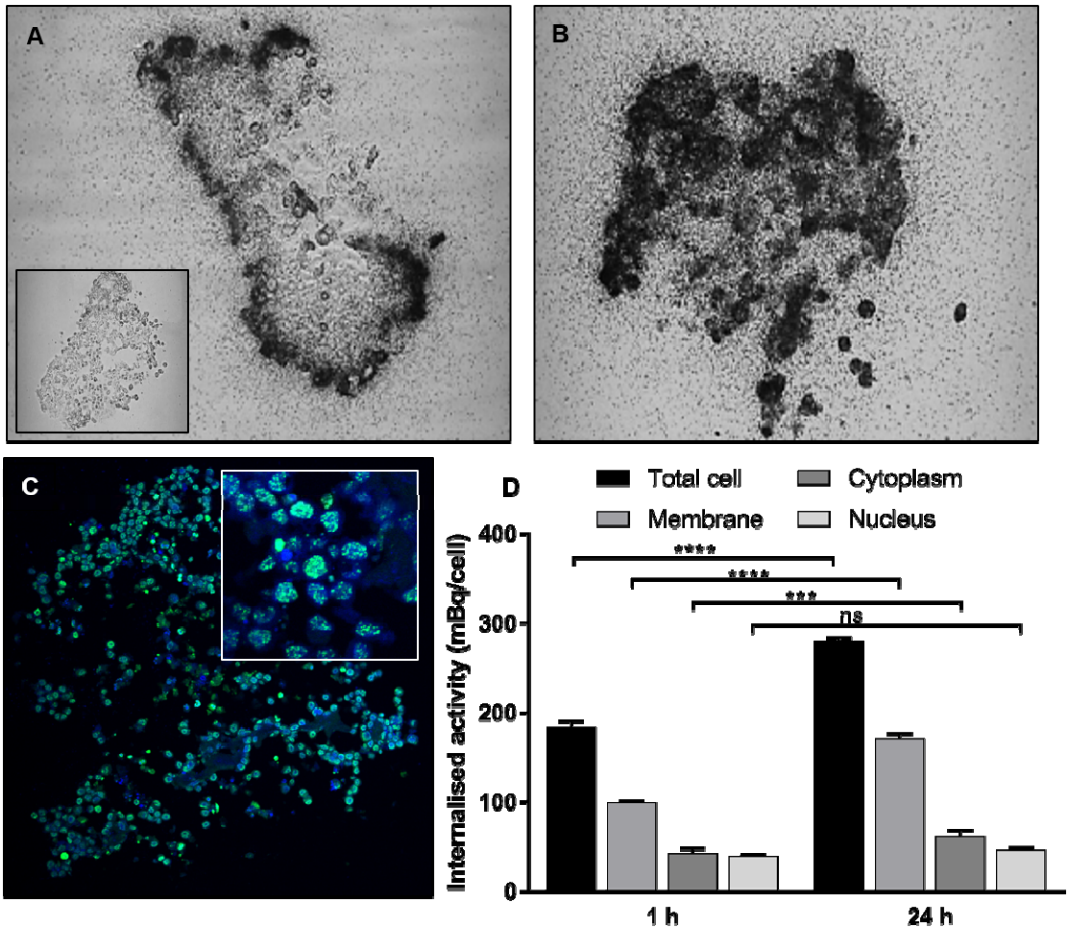
A
B
C
D
Total cell
Cytoplasm
Membrane
Nucleus
Internalised activity (mBq/cell)
400
300
200
100
0
****
****
***
ns
1 h
24 h

FIGURE 3.

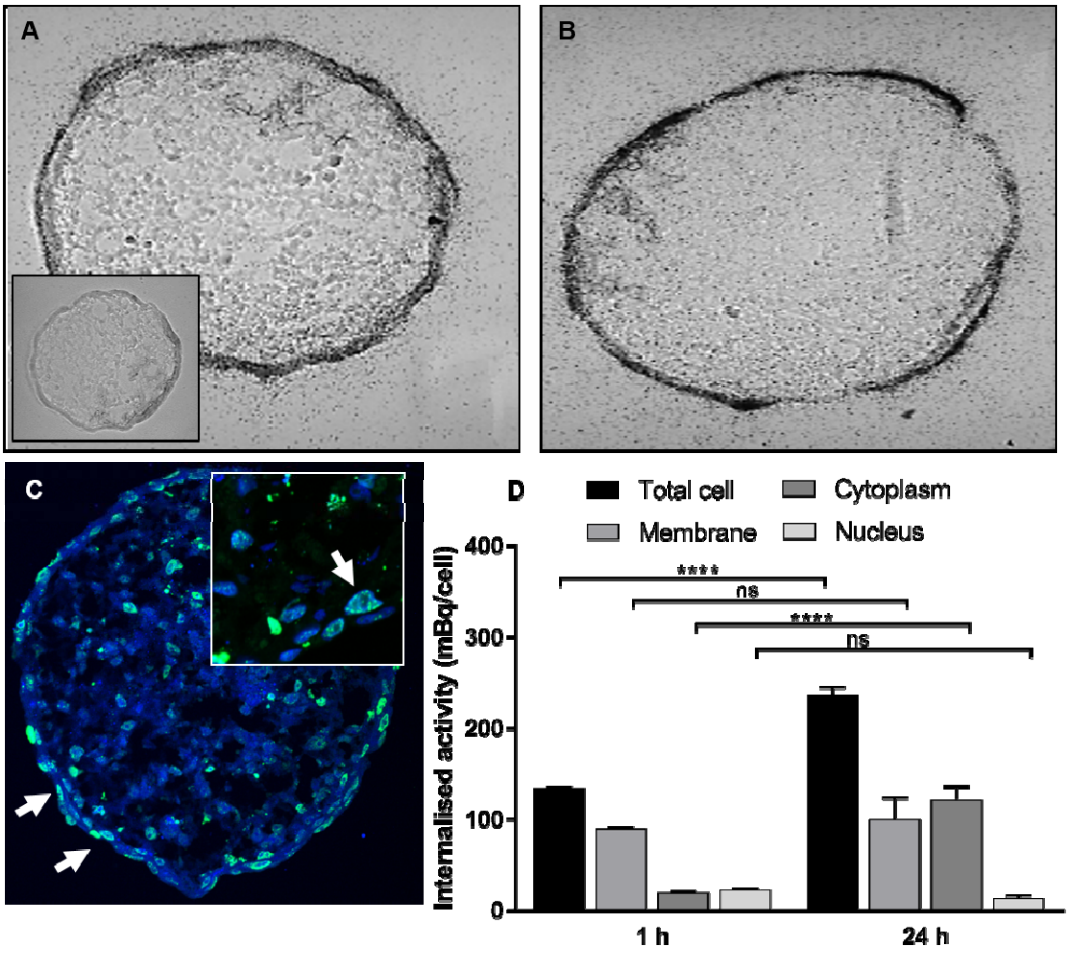
A
B
C
D
Total cell
Cytoplasm
Membrane
Nucleus
Internalised activity (mBq/cell)
400
300
200
100
0
****
ns
****
ns
1 h
24 h

FIGURE 4.

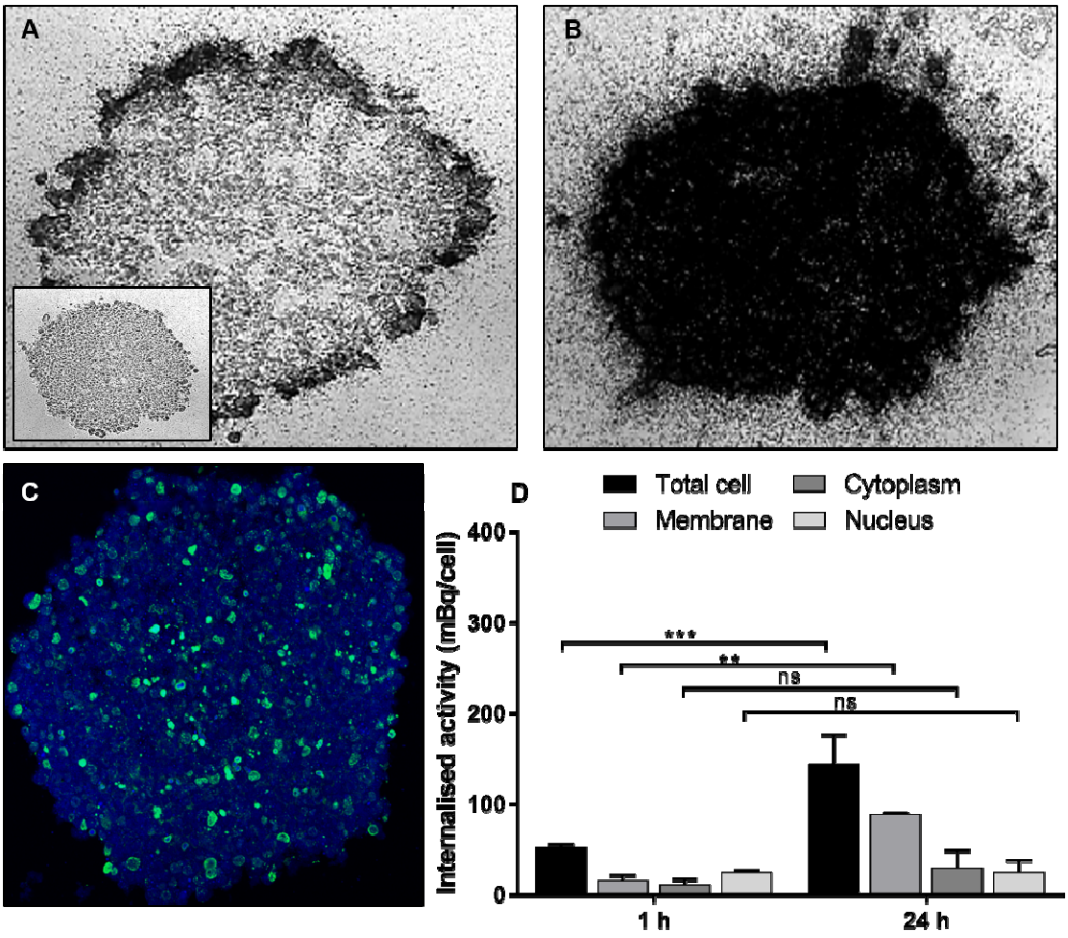
A
B
C
D
Total cell
Cytoplasm
Membrane
Nucleus
Internalised activity (mBq/cell)
400
300
200
100
0
***
**
ns
ns
1 h
24 h

FIGURE 5.

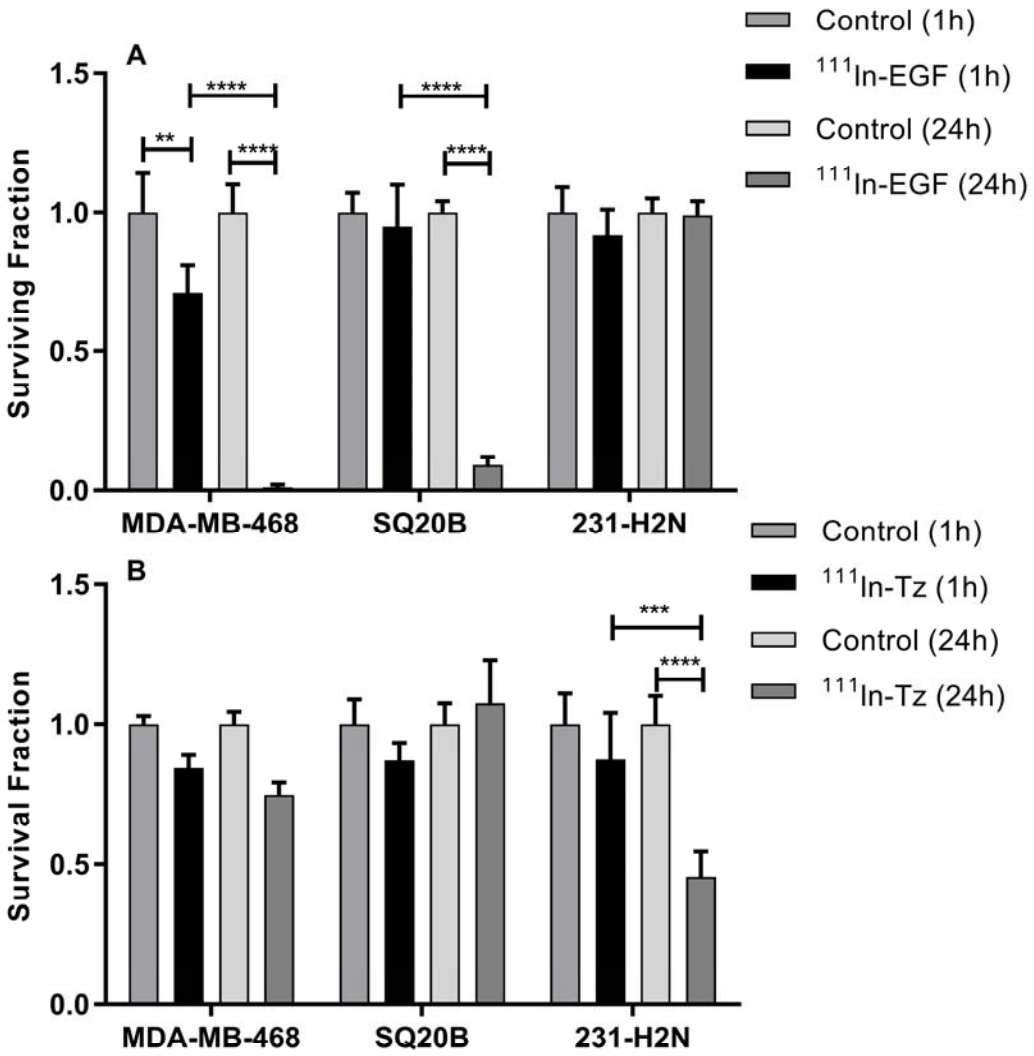
A
Surviving Fraction
1.5
1.0
0.5
0.0
**
****
****
****
****
MDA-MB-468
SQ20B
231-H2N
Control (1h)
111In-EGF (1h)
Control (24h)
111In-EGF (24h)
B
Survival Fraction
1.5
1.0
0.5
0.0
***
****
MDA-MB-468
SQ20B
231-H2N
Control (1h)
111In-Tz (1h)
Control (24h)
111In-Tz (24h)

FIGURE 6

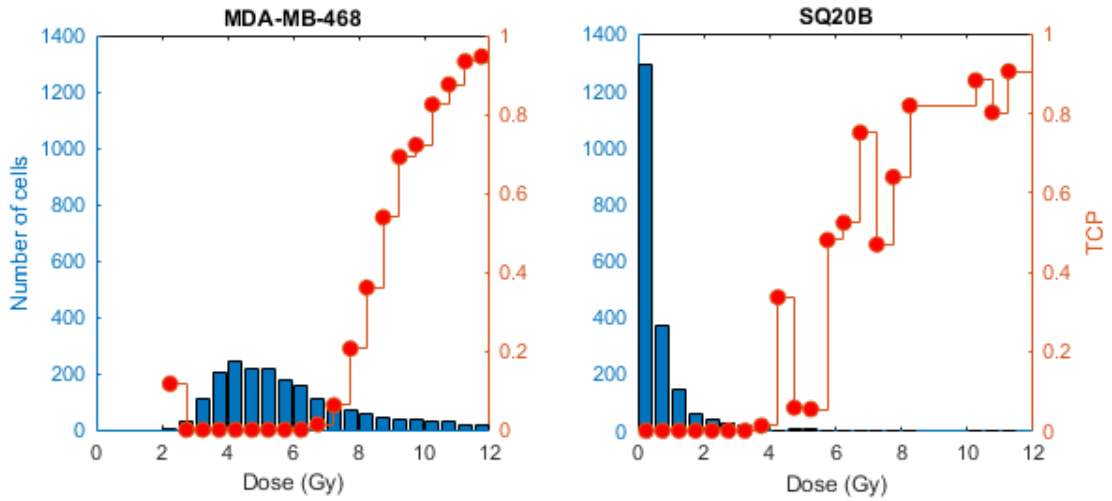
MDA-MB-468
SQ20B
Number of cells
TCP
Dose (Gy)
Dose (Gy)
0
200
400
600
800
1000
1200
1400
0
0.2
0.4
0.6
0.8
1
0
2
4
6
8
10
12

FIGURE 7.

TABLES

TABLE 1

Cellular *S*-values (Gy/Bq s) for different geometric models and cell lines.

	Single cells[a]			Monolayer[b]			Cluster – RCP[b]		
	S(N←N)	*S*(N←Cy)	*S*(N←Cs)	*S*(N←N)	*S*(N←Cy)	*S*(N←Cs)	*S*(N←N)	*S*(N←Cy)	*S*(N←Cs)
MDA-468	7.08E-04	8.47E-05	4.30E-05	9.83E-04 ±7.36E-04	1.53E-04 ±8.85E-05	1.04E-04 ±5.86E-05	1.07E-03 ±1.12E-03	1.94E-04 ±7.63E-05	1.42E-04 ±4.92E-05
SQ20B	4.21E-04	5.63E-05	3.21E-05	5.75E-04 ±3.63E-04	1.01E-04 ±2.84E-05	7.21E-05 ±2.06E-05	7.10E-04 ±8.30E-04	1.43E-04 ±5.95E-05	1.09E-04 ±3.93E-05
231-H2N	6.04E-04	5.35E-05	2.01E-05	1.01E-03 ±1.33E-03	1.19E-04 ±8.83E-05	6.98E-05 ±5.66E-05	1.02E-03 ±1.95E-03	1.45E-04 ±1.04E-04	9.49E-05 ±6.27E-05

[a]*S*-values of each cell line are determined by MC simulation for the average cell and nucleus radii given in Figure 2(D-F).
[b]Mean *S*-value ± SD, for varied cell/nuclei radii (packing ratio for RCP ≈ 0.17).

TABLE 2

Comparison of SF in ^{111}In-treated tumor spheroids.

		MDA-468		SQ20B		231-H2N	
		1 h	**24 h**	**1 h**	**24 h**	**1 h**	**24 h**
^{111}In-EGF	$\tilde{A}$ **cell (Bq s)**	331	19558	242	15594	13	1533
	$\tilde{A}$ **nucleus (Bq s)**	72	3688	42	1597	2	108
	SF_{exp}[b]	0.71(10)[c]	0.01(1)	0.95(15)	0.35(12)	0.92(9)	0.99(5)
	$SF_{MC(1)}$[d]	0.95	0.13	0.99	0.66	1.00	0.97
	$SF_{MIRDcell}$[e]	0.92	0.09	0.94	0.42	1.00	0.91
	$SF_{MC(2)}$[f]	0.87	0.01	0.98	0.43	1.00	0.93
	$SF_{MC(3)}$[g]	0.88	0.01	0.98	0.43	1.00	0.94
^{111}In-Tz	$\tilde{A}$ **(Bq s)**[a]	10	1026	14	1274	96	5947
	$\tilde{A}$ **nucleus (Bq s)**	1	67	2	170	46	1884
	SF_{exp}[b]	0.97(5)	0.75(4)	1.10(6)	1.08(16)	0.87(17)	0.46(9)
	$SF_{MC(1)}$[d]	1.00	0.92	1.00	0.96	0.99	0.67
	$SF_{MIRDcell}$[e]	1.00	0.89	1.00	0.90	0.98	0.69
	$SF_{MC(2)}$[f]	1.00	0.84	1.00	0.91	0.97	0.19
	$SF_{MC(3)}$[g]	1.00	0.85	1.00	0.91	0.97	0.38

[a] $\tilde{A}$ is derived from the mean whole-cell internalized activity using the trapezoidal integration.
[b] SF_{exp} derived from technical triplicates.
[c] 0.71(10) means 0.71±0.10.
[d] MC(1) is MC-derived SF based on the α and β values determined from ^{137}Cs irradiation.
[e] Calculated using the mean cell/nucleus radius. α and β values from ^{137}Cs irradiation are adopted for self and cross doses.
[f] MC(2) is similar to MC(1) but RBE=4 is applied to dose deposited by radiation sources in the nucleus (*33*,*34*).
[g] MC(3) is similar to MC(2) but Lea-Catcheside factor, G is applied. G=0.89 for cells incubated for 1 h. For cells incubated for 24 h, G for all cell lines are tabulated in Supplemental Table 2. All calculations assumed a repair half-time of 1.5 h.

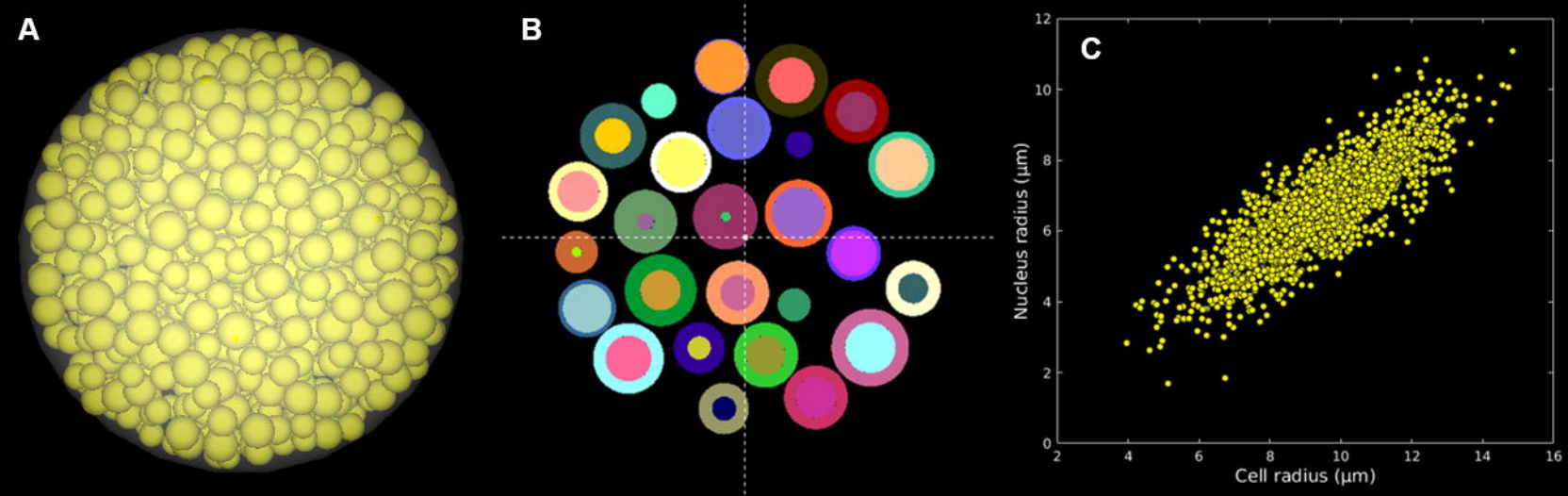
A
B
C
Nucleus radius (μm)
Cell radius (μm)
0
2
4
6
8
10
12
2
4
6
8
10
12
14
16

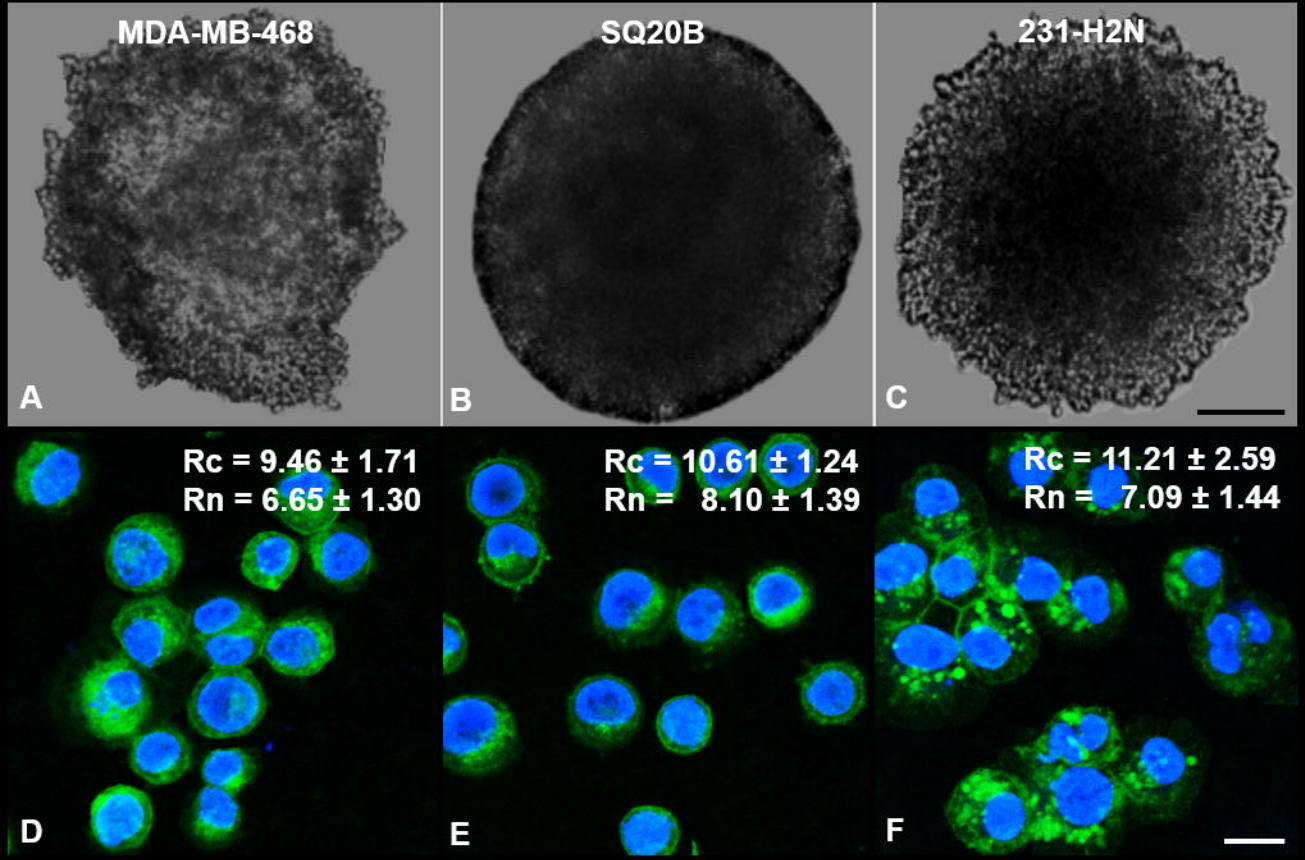
MDA-MB-468
SQ20B
231-H2N
A
B
C
Rc = 9.46 ± 1.71
Rn = 6.65 ± 1.30
Rc = 10.61 ± 1.24
Rn = 8.10 ± 1.39
Rc = 11.21 ± 2.59
Rn = 7.09 ± 1.44
D
E
F

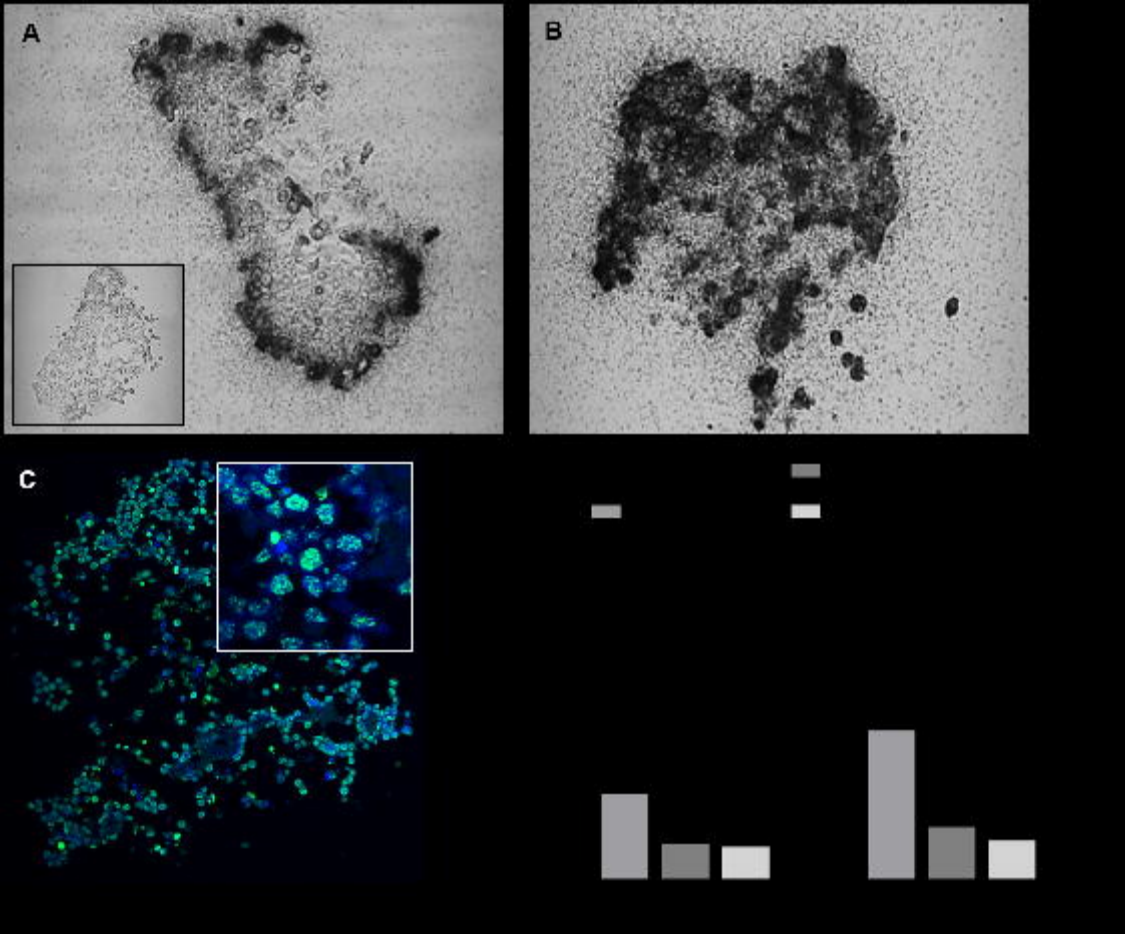
A
B
C

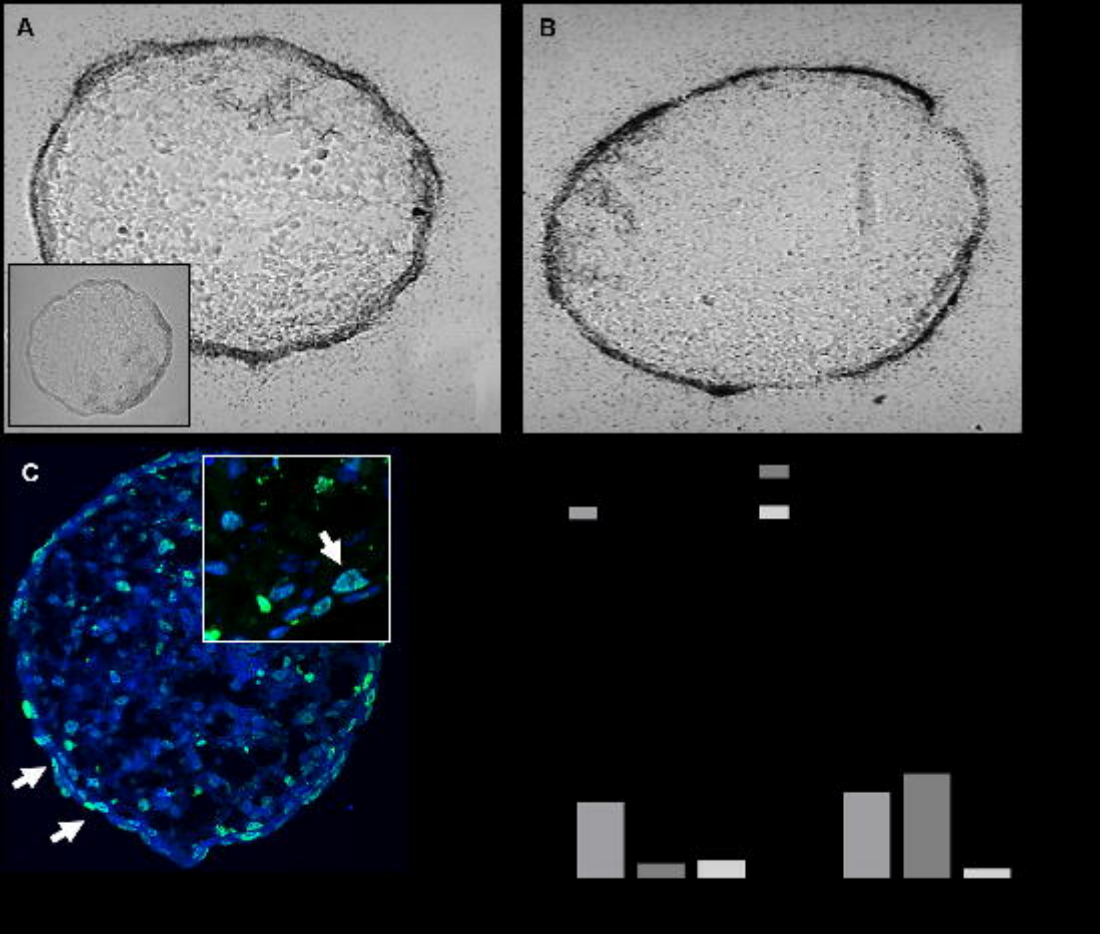
A
B
C

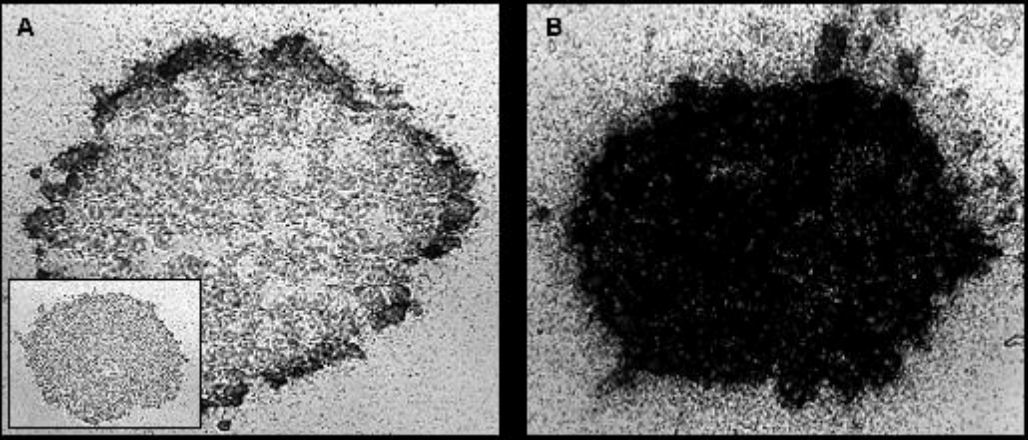
A
B

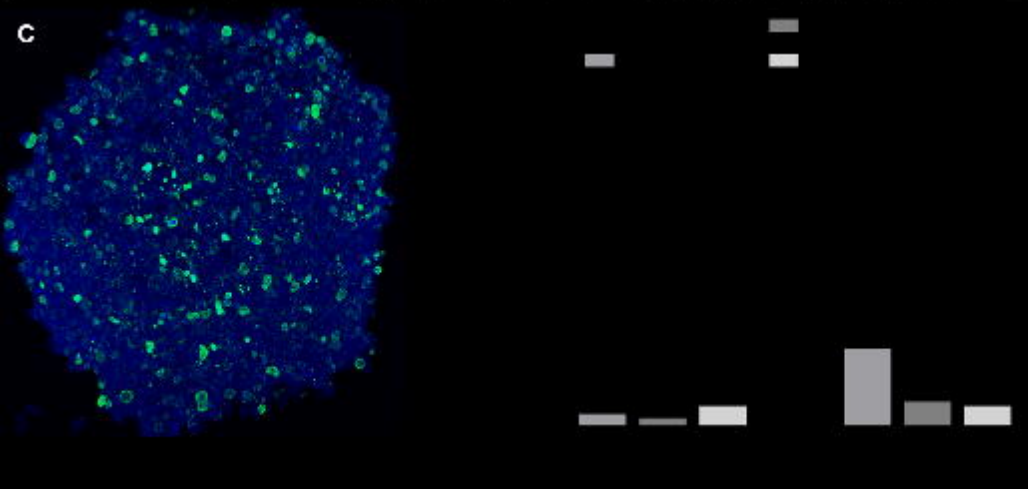
C

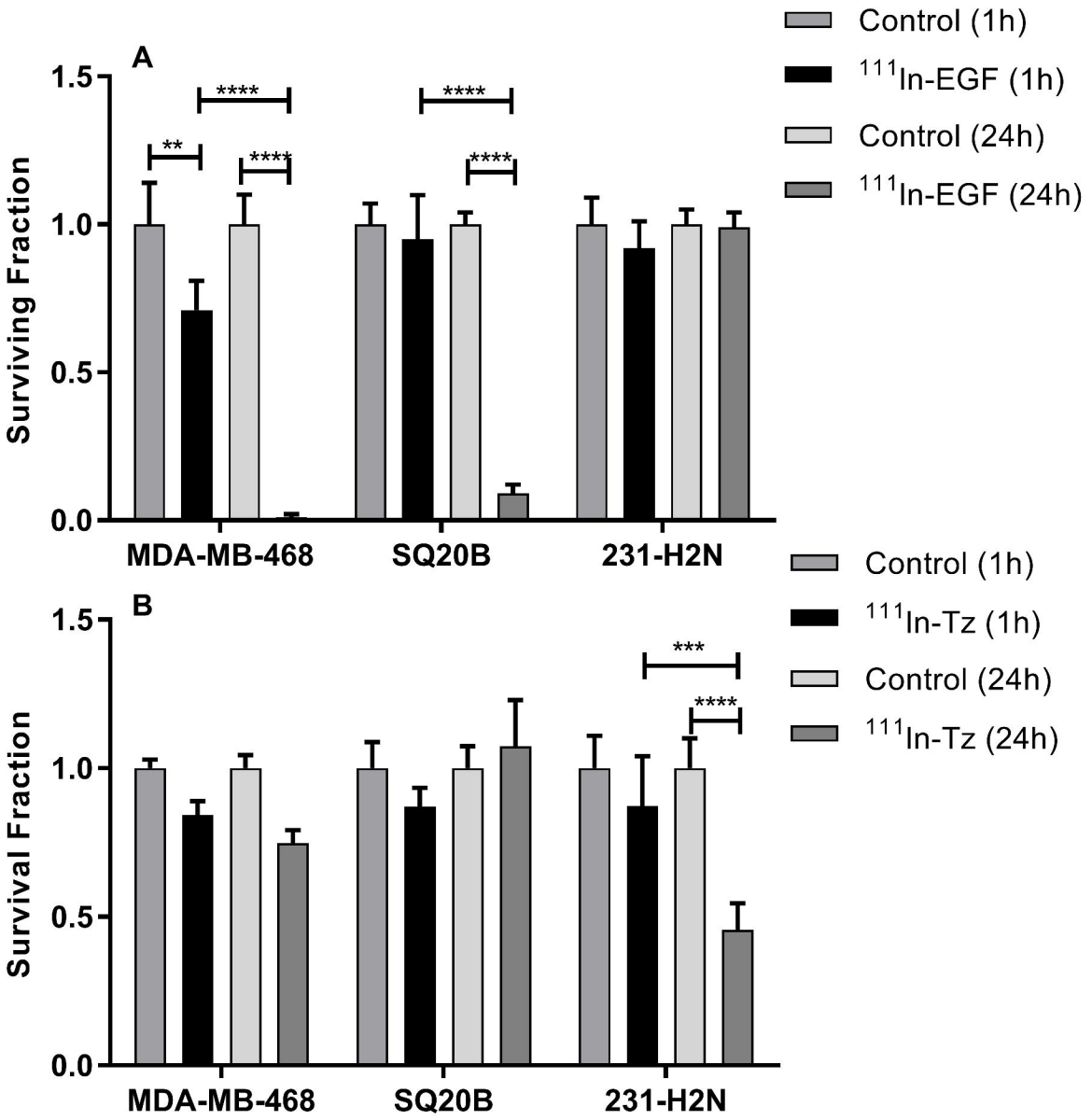
A
Surviving Fraction
1.5
1.0
0.5
0.0
**
****
****
****
****
MDA-MB-468
SQ20B
231-H2N
Control (1h)
111In-EGF (1h)
Control (24h)
111In-EGF (24h)
B
Survival Fraction
1.5
1.0
0.5
0.0
***
****
MDA-MB-468
SQ20B
231-H2N
Control (1h)
111In-Tz (1h)
Control (24h)
111In-Tz (24h)

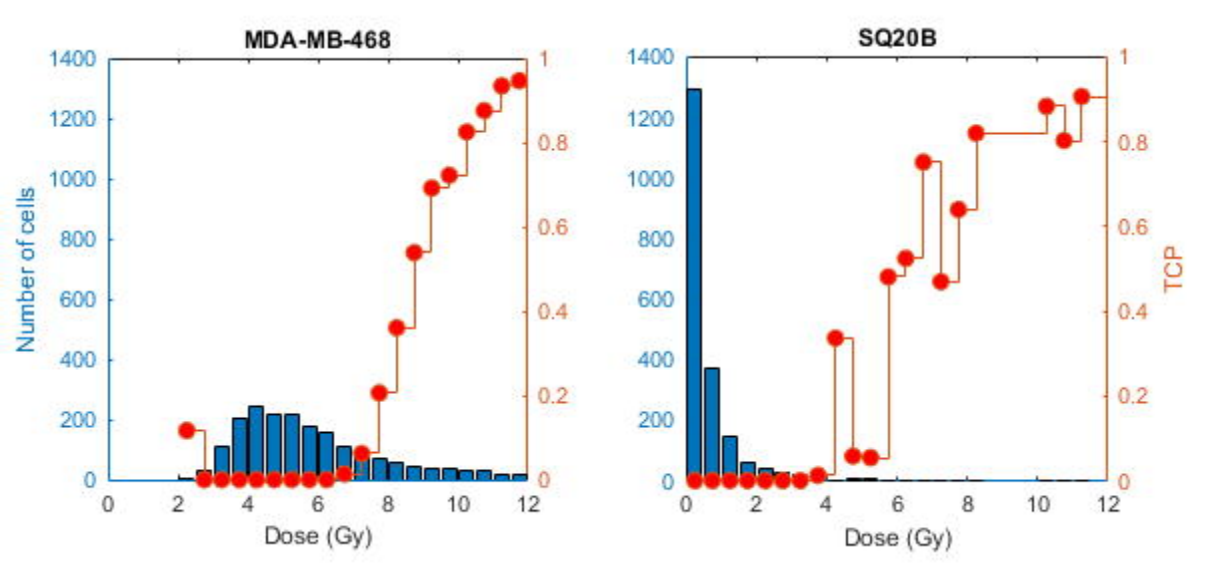
MDA-MB-468
SQ20B
Number of cells
TCP
Dose (Gy)
Dose (Gy)
0
200
400
600
800
1000
1200
1400
0.2
0.4
0.6
0.8
1
2
4
6
8
10
12